Journal of
Polymer Materials

Tech Science Press

Doi:10.32604/jpm.2025.059697

ARTICLE

Fabrication and Characterization of PANI/MgO NPs Composite Films for Photocatalysis Application

Malak Khannoucha[1,*], Boubekeur Boudine[1], Imene Ameur[1], Aouatef Dali[2], Ouahiba Halimi[1], Miloud Sebais[1] and Tahar Touam[3]

[1]Laboratoire de Cristallographie (LC), Faculté des Sciences Exacte, Université des frères Mentouri constantine 1, Constantine, 25000, Algérie

[2]Laboratoire des sciences et technologie de l'environnement (LSTE), Faculté des Sciences Exactes, Université de Constantine 1 frères Mentouri, Constantine, 25000, Algérie

[3]Laboratoire de Semiconducteurs, Université de Badji Mokhtar-Annaba, BP 12, Annaba, 23000, Algérie

*Corresponding Author: Malak Khannoucha. Email: khennouchamalak@gmail.com

Received: 15 October 2024; Accepted: 13 January 2025; Published: 27 March 2025

ABSTRACT: This work reports a soft chemistry approach for the synthesis of magnesium oxide nanoparticles (MgO) incorporated in a polyaniline (PANI) matrix to give PANI/MgO nanocomposite. Using spin coating method, three different percentages of MgO/PVC (1, 2, and 3% in wt.%) were deposited on glass substrates. These films of PANI/MgO nanocomposite were characterized by X-ray diffraction (XRD), atomic force microscopy (AFM), and UV-visible spectroscopy. The results of the XRD pattern revealed the embedding of MgO nanoparticles in the PANI matrix with cubic phase, with the average size of nanoparticles varying from 35.12 to 59.55 nm. The AFM images displayed a significant change in the morphology of the PANI/MgO NPs composite films as MgO concentration was increased. The optical transmittance analysis revealed that at very low concentrations of MgO in PANI/MgO nanocomposite films, there is a high transparency, reaching close to 90%. However, this transmittance decreases significantly as the concentration of MgO increases. The photocatalytic activity of the nanocomposite film was then evaluated for the degradation of methylene blue (MB) dye under UV light irradiation. The results indicated a strong potential for PANI/MgO nanocomposite films in effectively degrading MB, supported by a proposed mechanism for the photocatalytic reaction. Compared with other composites such as PVC/MgO, PANI/MgO nanocomposite presented better MB degradation efficiency.

KEYWORDS: Chemical synthesis; polyaniline/MgO composite films; photocatalysis

1 Introduction

Environmental pollution has recently become a major concern for humanity. More and more scientists are trying to find ways to overcome this problem. The increasing air and water pollution has motivated researchers to develop materials capable of degrading pollutants in the air and water [1,2]. Among these materials are semi-conducting oxides, which display high effectiveness in degrading dyes and organic species. Using semi-conducting oxides as photocatalysts is very effective in the degradation of organic pollutants and helps eliminate hazardous species in the air and in water with no secondary pollution [3,4]. Over the past few years, several semiconducting oxides, such as TiO_2, ZnO, MgO, SnO_2, ZnS, CdS, etc. [5,6], have been used as effective photocatalysts [7–9].

The incorporation of inorganic MgO-NPs into polymers results in notable changes in their behavior by altering their mechanical, electrical, optical, and photocatalytic properties [1]. The characteristics of the resulting material (nanocomposite) are influenced by the method of preparation and the relative concentrations of each component. This indicates that careful consideration of the synthesis techniques and the ratios of the materials are crucial for optimizing the performance of the nanocomposite. The elaboration of nanocomposites using transparent polymers as a host matrix and inorganic semiconducting NPs as charges is of great interest in several fields, such as optics, optoelectronics, solar energy, and air and water pollutant degradation. This kind of hybrid materials may inherit the benefits of both materials: the superior optoelectronic properties of polymers and the high electronic mobility of inorganic semiconductors [10].

Soft chemistry is an appropriate method to prepare polymer/semi-conducting oxide composites [11]. It consists of the introduction of the semi-conducting oxide *ex-situ* inside the polymer [12]. Among the polymers is polyaniline (PANI); it is a polymer made of amine and imine units which is mostly studied and used for its quality as an electronic conductor. This polymer may be prepared through two methods, one chemical [12] and the other electro-chemical [13]. Each method proceeds by oxidizing aniline in an acid environment. While the electrochemical method is useful to obtain polymer films, we usually use a chemical oxidant to easily produce large quantities of the polymer as a powder. In both cases, the end product is the result of a preferential head-to-tail coupling of the oxidized aniline molecules. In addition, PANI is a conducting polymer.

As mentioned above, semi-conducting oxide nanoparticles have shown good efficiency in degrading pollutants in water. Among the various oxide nanoparticles employed in photocatalytic processes, MgO has garnered significant attention due to its unique properties. Featuring a rock salt face-centered cubic (FCC) structure (NaCl type) with a unit cell dimension of 4.21 Å. MgO offers a wide band gap, exceptional thermal resilience, a low optical refractive index, and remarkable catalytic efficiency, porous structure, and potentially high specific surface area. These remarkable characteristics make MgO suitable for a broad spectrum of applications, including catalysis, wastewater treatment, antibacterial agents, additives in refractory materials, paints, antifungal agents, and ceramics [14,15]. Moreover, MgO has emerged as a highly effective material in photocatalysis, demonstrating the capability to efficiently degrade pollutants.

The structure and morphology of materials are primarily influenced by the elaboration conditions. In terms of preparation methods, several protocols have been developed for synthesizing MgO nanoparticles, including the sol-gel method [16,17], co-precipitation [18], thermal decomposition [19], chemical vapor deposition [20], ultrasonic spray pyrolysis [8,21], microwave synthesis [22], hydrothermal synthesis [23], and green synthesis [24]. Among these, the sol-gel method was selected for this study due to its simplicity and cost-effectiveness. This method allows for precise control over the composition and properties of the nanoparticles, making it an attractive option for producing high-quality MgO nanoparticles.

The introduction of MgO into PANI was performed using soft chemistry.

This article aims to present a preparation method for MgO nanoparticles through the sol-gel method and to study the impact of the MgO-NPs as a doping agent at small concentrations (1%, 2%, and 3%) on the photocatalytic characteristics of the PANI/MgO-NPs composite films. In existing research, we do not find many studies on the photocatalytic degradation of organic pollutants by PANI/MgO-NPs composites. Furthermore, to date, there have been no studies examining the influence of different concentrations of MgO in PANI on the photocatalytic properties of PANI/MgO NPs composites employing methylene blue dye exposed to UV light.

2 Experimental Procedure

2.1 Materials Used

For the preparation of PANI and MgO NPs, we used the following materials Ammonium persulfate ($(NH_4)_2S_2O_8$), hydrochloric acid (HCl), aniline (C_6H_5-NH_2), Magnesium acetate tetrahydrate (Mg $(CH_3COO)_2 \bullet 4H_2O$), anhydrous ethanol ($C_2H_5OH$), and oxalic acid dihydrate ($C_2H_2O_4 \bullet 2H_2O$). All products are purchase from SIGMA ALDRICH.

2.2 Sol-Gel Synthesis of MgO-NPs

The sol-gel technique has been used to create MgO NPs. The solution was prepared using the following precursors: anhydrous ethanol (C_2H_5OH) as a solvent; magnesium acetate tetrahydrate (Mg $(CH_3COO)_2 \bullet 4H_2O$) as a source of magnesium; and oxalic acid dihydrate ($C_2H_2O_4 \bullet 2H_2O$) as a complexing agent. Initially, anhydrous ethanol was used to dissolve the magnesium acetate tetrahydrate while stirring. Next, 1 mol of oxalic acid was added to the solution to raise its pH to 5. A thick white gel formed after the solution was stirred magnetically for one hour at room temperature. After being exposed overnight, the resulting white gel was dried for 24 h at 100°C in an oven. Using amarble pestle and mortar, the resulting material was ground to create a finely ground powder. Ultimately, MgO NPs were created by annealing the fine powder at 950°C [25].

2.3 Synthesis of Polyaniline (PANI) and the PANI/MgO Composite

Emeraldine salt (PANI) was synthesized at room temperature in an ethylene glycol bath using the following procedure: bottle A, containing 40 mmol of aniline, was dissolved in 100 mL of 1 mol of HCl and kept at room temperature for 1 h. The oxidizing agent solution was prepared by dissolving 50 mmol of ammonium persulfate (APS) in 100 mL of demineralized water (bottle B) and kept at (the same) room temperature for 1 h. The polymerization process began by introducing the oxidizing agent solution into an aniline hydrochloride solution, rapidly mixing the resulting solution, and then keeping it at the desired polymerization temperature. Polymerization was left to proceed for up to 24 h to ensure that the aniline monomer was converted into PANI. The composite was got by adding to the obtained PANI solution the MgO solution prepared by dissolving MgO in HCl at concentrations of 1%, 2% and 3% by volume (soft chemistry method). This method did not require stabilization of the solution and is carried out at room temperature.

Finally, pure ES-PANI and composite PANI/MgO (1, 2, and 3 wt.%) films were deposited onto substrates of glass by spin-coating using a syringe, a drop of the solution was deposited onto a glass slide. The slide is mounted on a motorized axle that rotates at a speed ranging from 300 to 3000 rpm for 45 s; the obtained samples have a greenish color.

2.4 Characterization Techniques

The prepared samples of pure PANI and PANI/MgO films (with MgO concentrations of 1, 2, and 3 wt.%) were characterized using various analytical techniques. Structural analysis was performed using X-ray diffraction (XRD), with data collected on a PANalytical X'Pert Pro diffractometer equipped with a Cu Kα radiation source (wavelength 0.15406 nm). The surface morphology of the samples was examined using Atomic Force Microscopy (AFM, PHEWE). Additionally, the optical transmittance spectra were recorded using a UV-3101 PC-Shimadzu double-beam spectrophotometer.

2.5 Photocatalysis Procedure

The photocatalytic performance of the pure PANI and PANI/MgO-NPs films was analyzed by investigating the photodegradation MB dye when subjected to UV exposure at ambient temperature. Films of PANI/MgO-NPs (MgO: 0, 1, 2, and 3 wt.%) were placed in Petri dishes containing 50 mL of an aqueous MB solution with an initial concentration c_0 of 10^{-5} M.

Before UV irradiation, the MB solutions were mixed for 30 min in a light-free environment to facilitate the establishment of adsorption-desorption equilibrium between the organic dye and the surface of the catalyst. To isolate the effect of the catalyst, control experiments were conducted by irradiating MB solutions without any samples under identical conditions. The Petri dishes with the composites and MB solution were exposed to UV light using a monochromatic UV lamp with a wavelength of 365 nm (3.39 eV) and a power output of 15 W, positioned 8 cm above the solution surface. During irradiation, 4 mL aliquots of the solution were extracted from the reactor at 10-min intervals to record absorbance spectra using a dual-beam Shimadzu UV-301 PC spectrophotometer. The MB concentration was evaluated based on a standard curve that establishes a relationship between concentration and optical absorbance. The degradation efficiency (ρ) of MB was determined using the following formula [26]:

$$\rho = \left(1 - \frac{c}{c_0}\right) \times 100\% \tag{1}$$

3 Results and Discussion

3.1 XRD and EDX Characterization

Fig. 1A shows the XRD spectrum of the MgO nanoparticles. Diffraction peaks were observed at 2θ = 36.76, 42.86, 62.24, 74.83, 78.70. These peaks correspond to the diffraction from the (111), (200), (220), (311), and (222) planes, characteristic of the cubic crystalline phase of MgO (JCPDS no. 45-0946).

The average crystallite size (D, in nm) was calculated using Scherrer's formula. Additionally, the lattice parameter (a), the mean inhomogeneous strain (e), and the residual stresses (σ, in GPa) were determined using the following equations [27,28]:

$$D = \frac{0.9\lambda}{\beta \cos\theta} \tag{2}$$

$$d_{hkl} = \frac{a}{\sqrt{h^2 + k^2 + l^2}} \tag{3}$$

$$\varepsilon = \frac{\beta \cos\theta}{4} \tag{4}$$

$$\sigma = \varepsilon E \tag{5}$$

Here, λ, β, θ, and E represent the wavelength of the X-rays ($\lambda_{Cu\ K\alpha}$ = 0.15402 nm), the full width at half maximum (FWHM) of the diffraction peak, the Bragg diffraction angle, and the Young's modulus of MgO (E = 300 GPa), respectively. The results are grouped in Table 1.

Fig. 1B shows the XRD spectra of the PANI/MgO-NPs (0%, 1%, 2%, and 3%) composites. The diffractogram of pure PANI (Fig. 1B) exhibits three more or less narrow and intense peaks located at 2θ = 8, 15, 20, and 25°. The shape of these peaks suggests partial order in the material and points to a semi-crystalline structure for PANI.

Fig. 1C shows the XRD spectra of the PANI/1% MgO-NPs (Fig. 1Ca), PANI/2% MgO-NPs (Fig. 1Cb), and ES-PANI/3% MgO-NPs (Fig. 1Cc) composites.

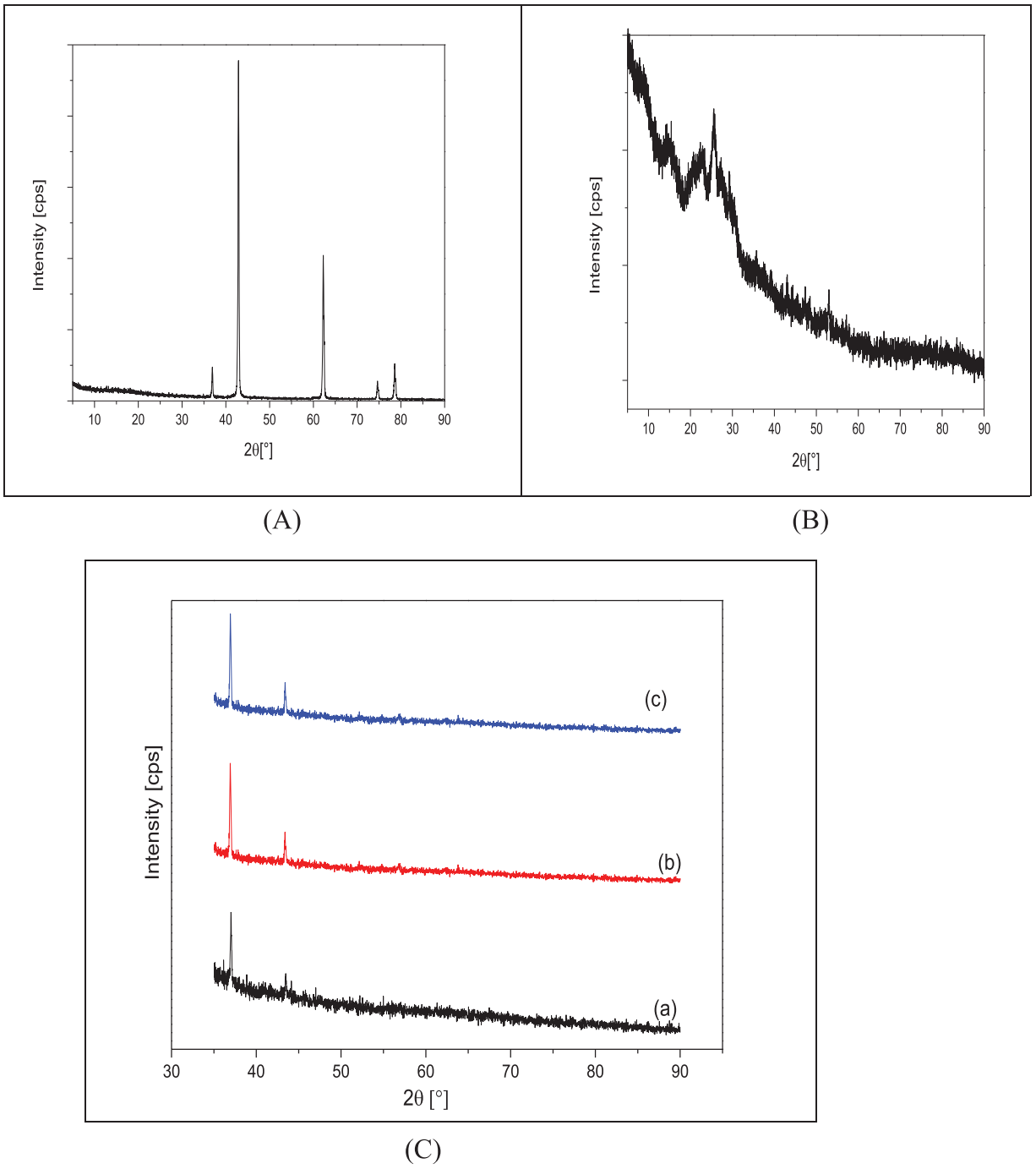

Figure 1: XRD pattern of (A) XRD pattern of MgO, (B) XRD pattern of undoped PANI, (C) XRD patterns of (a) PANI/1% of MgO NPS, (b) PANI/2% of MgO NPS and (c) PANI/3% of MgO NPS

Table 1: Average size, mean strain, residual stresses, and lattice parameter of MgO NPs

2θ (°)	θ (°)	d_{hkl} (A)	β (°)	D (nm)	$\varepsilon \times 10^{-4}$	σ (Gpa)	a (A)
36.91	18.45	2.43	0.25026	33.47	10	0.32	4.21
42.89	21.44	2.10	0.26957	31.66	11	0.35	4.21
62.24	34.14	1.37	0.34259	28.01	14	0.44	3.88
74.68	37.34	1.27	0.39825	25.09	17	0.52	4.21
78.62	39.31	1.21	0.42085	24.39	18	0.55	4.21

We observe that the crystallization of MgO improves as its concentration increases within the composite. On all three spectra, we observe peaks located around 2θ = 36.91 and 42.89°, corresponding to diffractions from the (111) and (200) planes, respectively (Table 2). We notice a slight discrepancy in the peak positions relative to those reported on JCPDS card no. 45-0946. Since the lattice parameter, a, of the various MgO NPs inside the PANI is smaller than the one reported on JCPDS card no. 00-045-0946, the discrepancy in peak positions is probably due to the contraction of the MgO lattice in the composite. While the most intense peak reported on JCPDS card no. 00-045-0946 corresponds to the (200) plane; all the XRD spectra of the PANI/MgO-NPs (1%, 2%, and 3%) composites show that the diffraction from the (111) plane produces the most intense peak. Thus, the composites exhibit a preferential orientation parallel to the (111) plane [28]. We also note that the sizes of the MgO particles inside the composites are nanometric.

Table 2: Average size, mean strain, residual stresses, and lattice parameter of PANI end PANI/(1%, 2%, and 3%) MgO NPs composite films

Sample	2θ (°)	θ (°)	d_{hkl} (A)	(hkl)	β (°)	D (nm)	$\varepsilon \times 10^{-4}$	σ (Gpa)	a (A)
PANI/1% MgO NPs	37.02	18.51	2.42	(111)	0.15968	52.47	6.6	0.19	4.20
	43.48	21.74	2.08	(200)	0.14364	59.55	5.8	0.17	4.16
PANI/2% MgO NPs	36.95	18.47	2.43	(111)	0.17692	47.35	7.3	0.21	4.21
	43.4	21.70	2.08	(200)	0.18215	46.94	7.3	0.22	4.16
PANI/3% MgO NPs	37.16	18.58	2.41	(111)	0.21143	39.64	8.7	0.26	4.18
	43.43	21.71	2.08	(200)	0.24352	35.12	9.8	0.29	4.16

The X-ray energy dispersive analysis (EDX) performed on the PANI and PANI/(1%, 2%, and 3%) MgO nanoparticles composite films (Fig. 2) in addition to the elements constituting the glass substrate, the presence of carbon, manganese, and oxygen. This finding confirmed the successful incorporation of MgO nanoparticles into the polyaniline matrix. Moreover, this result aligns well with the structural information obtained from the XRD analysis.

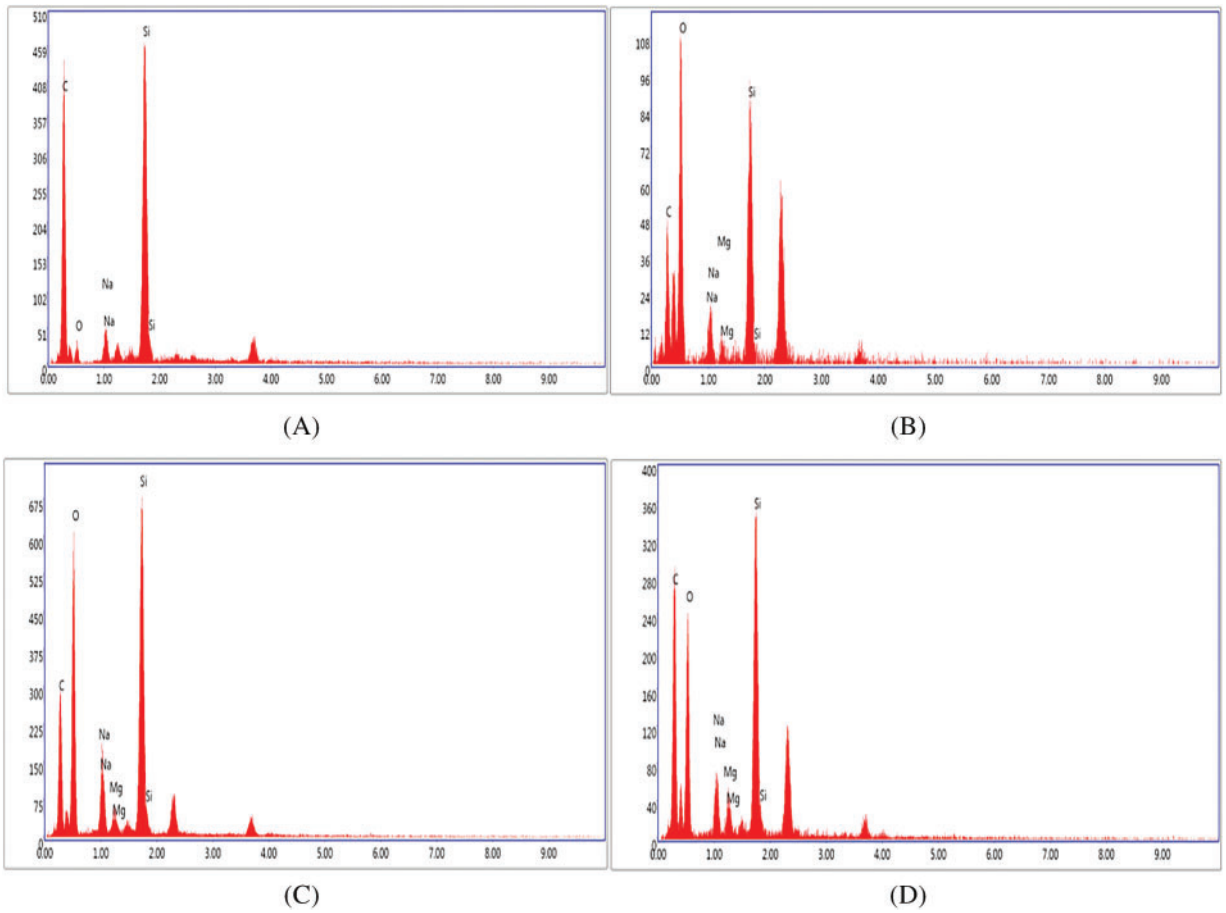

Figure 2: EDX spectra of (A) undoped PANI, (B) PANI/1% of MgO NPS, (C) PANI/2% of MgO NPS and (D) PANI/3% of MgO NPS

3.2 Morphological Characterization

The surface morphology of PANI/MgO-NPs composite films was studied by AFM. Fig. 3 displays the AFM of the PANI/MgO-NPs composite films deposited onto glass substrates.

We noted a significant change in the morphology of the PANI/MgO NPs composite films as MgO concentration was increased. As the surface of polymers was formed by pores, this change was caused by the manner of filling these pores. It was observed that all obtained films had a polycrystalline nature. The AFM images of PANI/MgO-NPs composite films showed that the grains were irregular in shape. The distribution of the crystallites on the surface morphology was inhomogeneous.

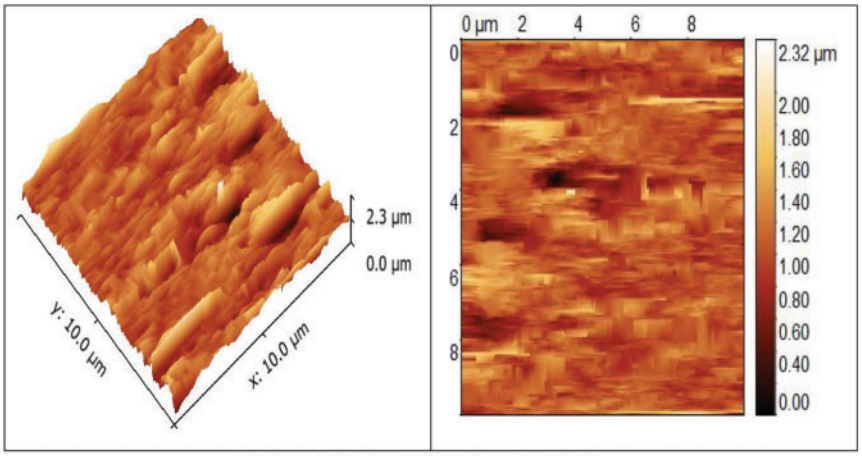

(A) IMAGES of PANI / 1% of MgO NPS

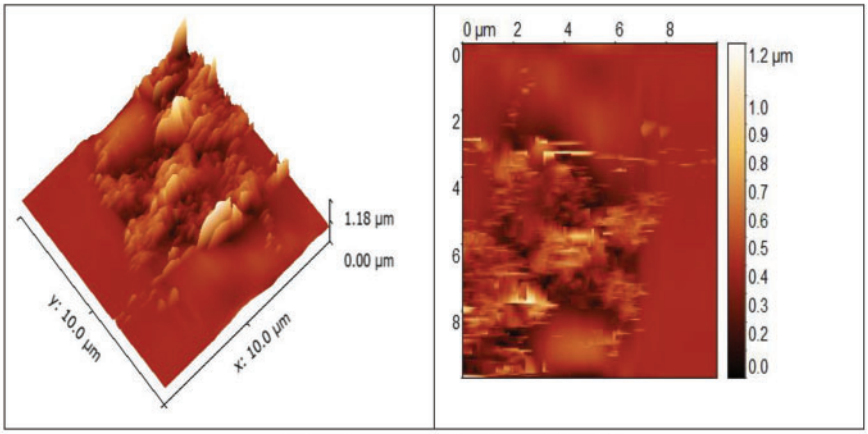

(B) Images of PANI / 2% of MgO NPS

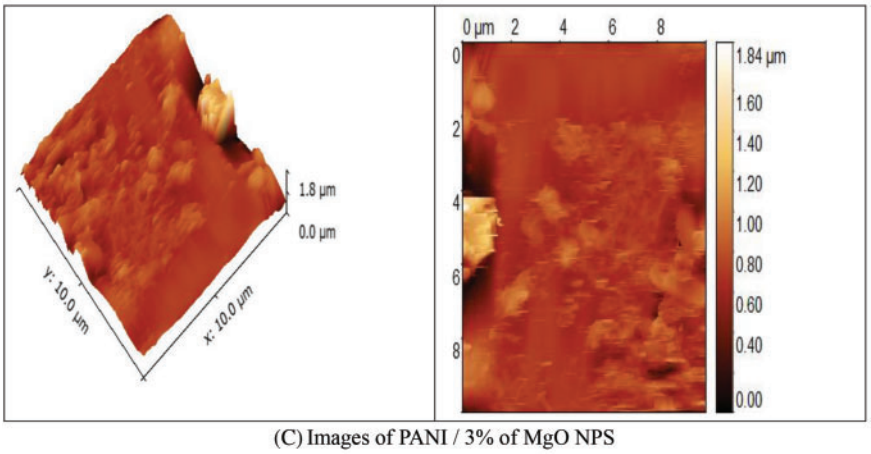

(C) Images of PANI / 3% of MgO NPS

Figure 3: AFM image of (A) PANI/1% of MgO NPs, (B) PANI/2% of MgO NPs and (C) PANI/3% of MgO NPs composite films

3.3 Optical Characterization

The optical transmittance measurements, of PANI/MgO-NPs composite films, were performed at ambient temperature across a wavelength range of 300 to 800 nm (Fig. 4). The transmittance spectrum of PANI/MgO-NPs composite films, specifically those doped with 1% MgO NPs, demonstrated very high transparency in the visible region, reaching approximately 90%. Additionally, these films exhibited strong absorption in the UV range. In contrast, the PANI/MgO NPs composite films with 2% and 3% MgO NPs showed a significant decrease in transmittance in the visible region, dropping to about 40%. The absorption edge detected in the UV region near $\lambda \sim 355$ nm suggests that the MgO nanoparticles possess a broad optical bandgap. Additionally, as the concentration of MgO NPs increased, the absorption edge exhibited a slight blue shift towards shorter wavelengths, indicating higher energy absorption. This behavior aligns well with the findings from X-ray diffraction (XRD) analysis.

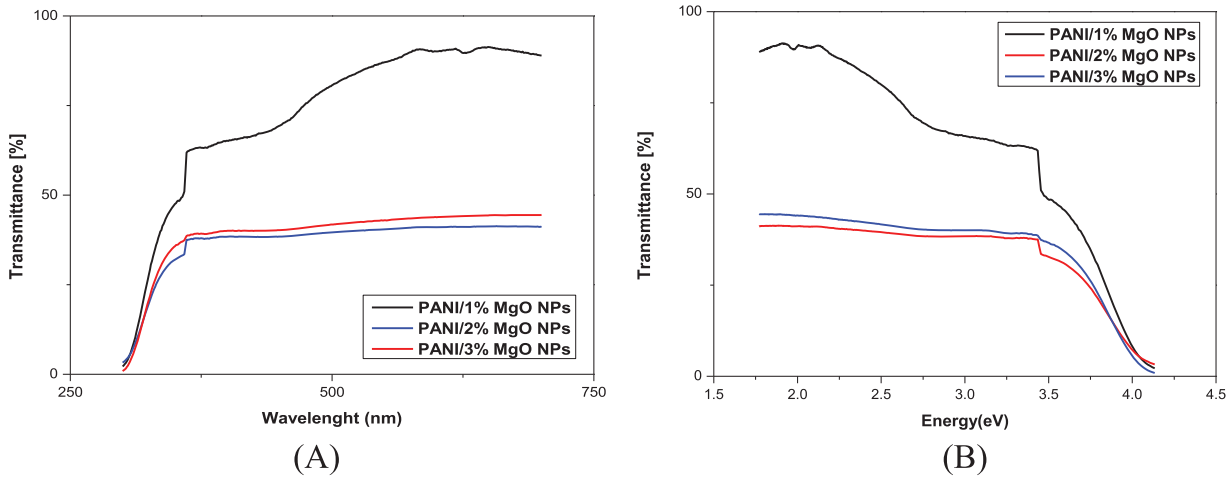

Figure 4: Transmittance spectra of PANI/MgO NPs (1%, 2%, and 3%) vs. (A) wavelength (B) energy

To estimate the band-gap energy of PANI/MgO-NPs composite films from the absorption spectra, the Tauc formula was employed, as MgO is known to be a direct band-gap semiconductor.

$$(\alpha h\nu)^2 = B(h\nu - E_g) \tag{6}$$

When $(\alpha h\nu)^2 = 0$, it indicates that the band-gap energy (E_g) is equal to $h\nu$. By extending the linear portion of the graph of $(\alpha h\nu)^2$ against photon energy ($h\nu$) along the horizontal axis, we can determine the value of the band-gap energy E_g. Fig. 5 illustrates this extension of the $(\alpha h\nu)^2$ curves plotted against photon energy ($h\nu$).

The estimated values of the optical band gap energy for MgO at concentrations of 1%, 2%, and 3% by weight embedded in ES-PANI are presented in Table 2. It was observed that the band-gap energy ranged from 3.49 to 3.60 eV.

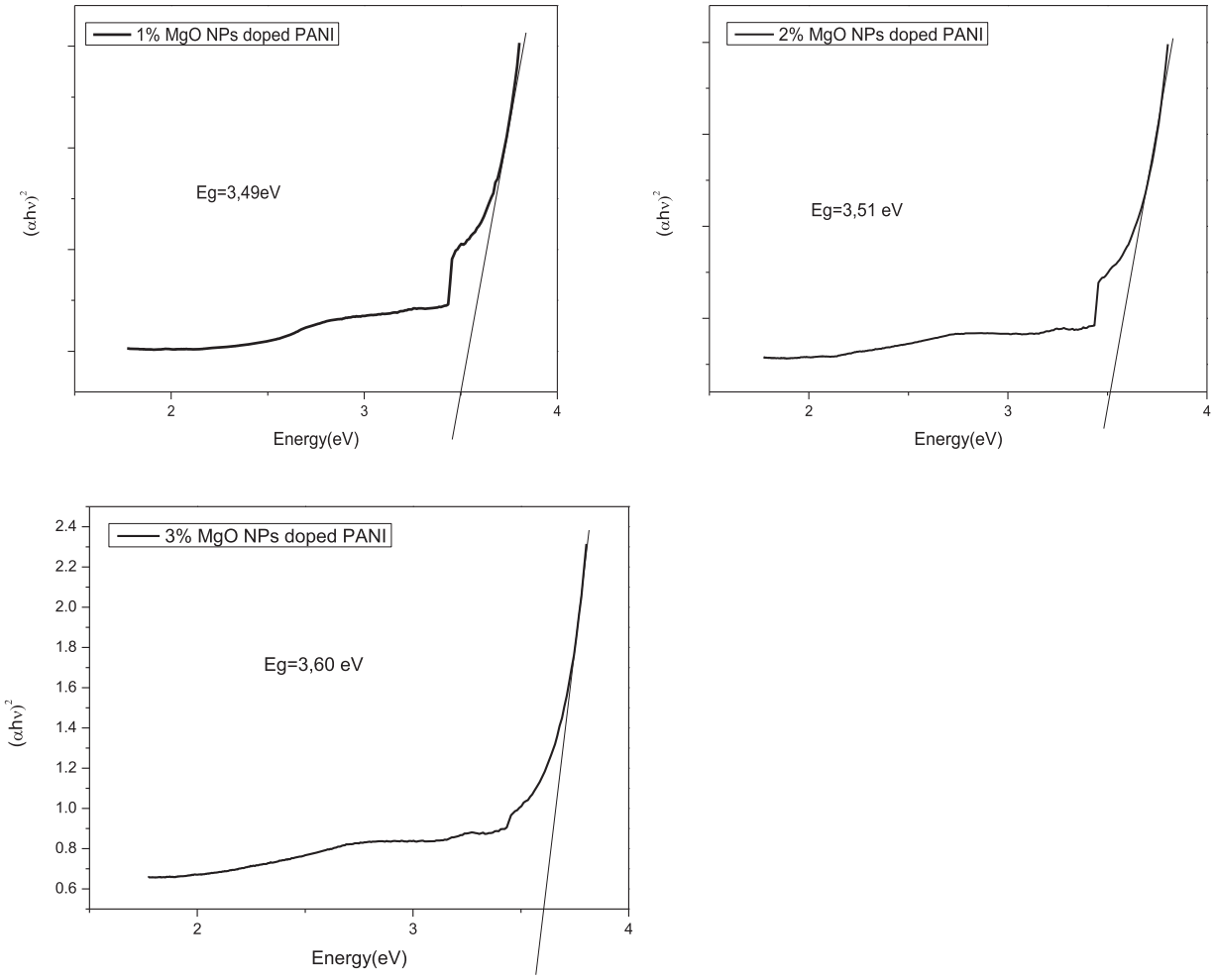

Figure 5: $(\alpha h\nu)^2$ vs. energy

3.4 Photocatalytic Activity

The photocatalytic activity of PANI and MgO (1%, 2% and 3%) nanoparticles doped PANI thin films were evaluated for the degradation of methylene blue (MB) dye under UV irradiation. The thin films were placed in a container holding 50 mL of a methylene blue (MB) solution in water with a starting concentration of approximately 10^{-5}M. The photocatalytic activity was assessed by monitoring the changes in optical absorption of the solution over different time intervals in relation to wavelength, ranging between 400 to 800 nm. No significant degradation of MB was observed in the absence of PANI and MgO nanoparticles doped at 1%, 2%, and 3% by weight under UV irradiation, as shown in Fig. 6.

Fig. 7A–D illustrates the UV-Vis absorption spectra of the MB solution in water, both without and with the addition of PANI and MgO (1%, 2%, and 3%) nanoparticles doped PANI thin films under exposure to UV irradiation of 365 nm (3.4 eV) which agrees with the bandgap energy of the fabricated PANI/MgO-NPs composite films.

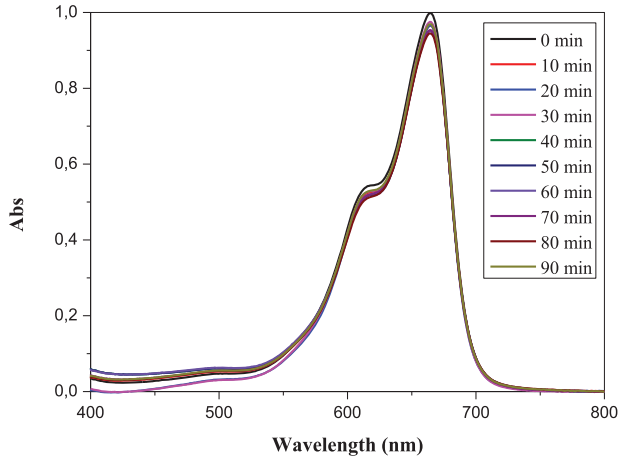

Figure 6: Absorption spectra of the MB solution in an aqueous medium subjected to ultraviolet irradiation

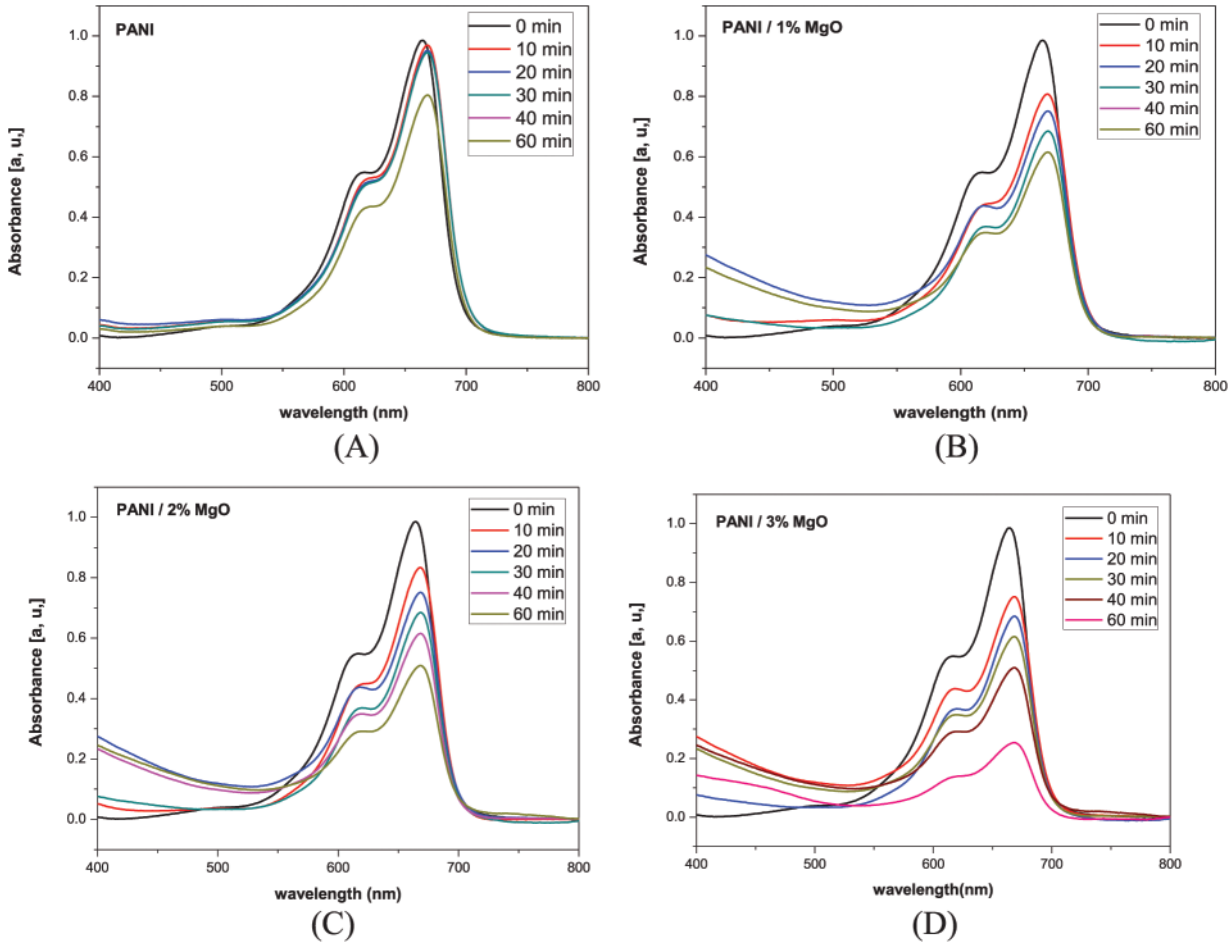

Figure 7: Absorption spectra of the MB solution in water subjected to ultraviolet exposure of (A) pure PANI (B) PANI/1% of MgO NPs (C) PANI/2% of MgO NPs, and (D) PANI/3% of MgO NPs

The absorption data in the presence of UV light were collected at 10-min intervals for a total duration of 60 min. To monitor the temporal changes in absorption, we chose the maximum absorption at 664 nm. It was observed that MB was degraded as soon as PANI and MgO (1%, 2%, and 3%) nanoparticles doped PANI have been set within the solution.

The absorbance of the solution could be expressed by the percentage degradation of MB ρ:

$$\rho = \left(1 - \frac{c}{c_0}\right) \times 100\%$$

where C was the concentration at time t and C_0 was the concentration at $t = 0$. This ρ was calculated for the four samples in relation to the exposure duration. Fig. 7 illustrates the reduction rate (ρ) of MB in the mixtures over the duration of exposure.

Various observations could be made. MB showed no signs of degradation without PANI and MgO (1%, 2%, and 3%) NPs doped PANI thin films under UV irradiation (Fig. 8A). The minor reduction in the measured concentration of MB can be attributed to the photolysis of MB in water. It was noted that MB begins to degrade immediately upon the introduction of PANI and MgO (1%, 2%, and 3%) NPs doped PANI thin films into the solution. These findings enable us to rule out the influence of UV light on the observed degradation of MB. Following 60 min, ρ of PANI is 20% while PANI/MgO NPs (3 wt.%) was about 80%. In our previous work, the MB degradation by MgO doped polyvinyl chloride (PVC) composite reached 40% in 150 min [11], while for the case of Mg-doped ZnO nanopowder atteined 80% in 150 min [27]. This made the PANI/MgO NPS composite interesting for photocatalysis. So, adding MgO NPs to the PANI has a significant effect. On closer inspection, we could also see that the MB degradation dynamics was distinguished based on the concentration of MgO nanoparticles. The maximum level of MB degradation was observed for PANI/MgO NPs (3% in wt.%).

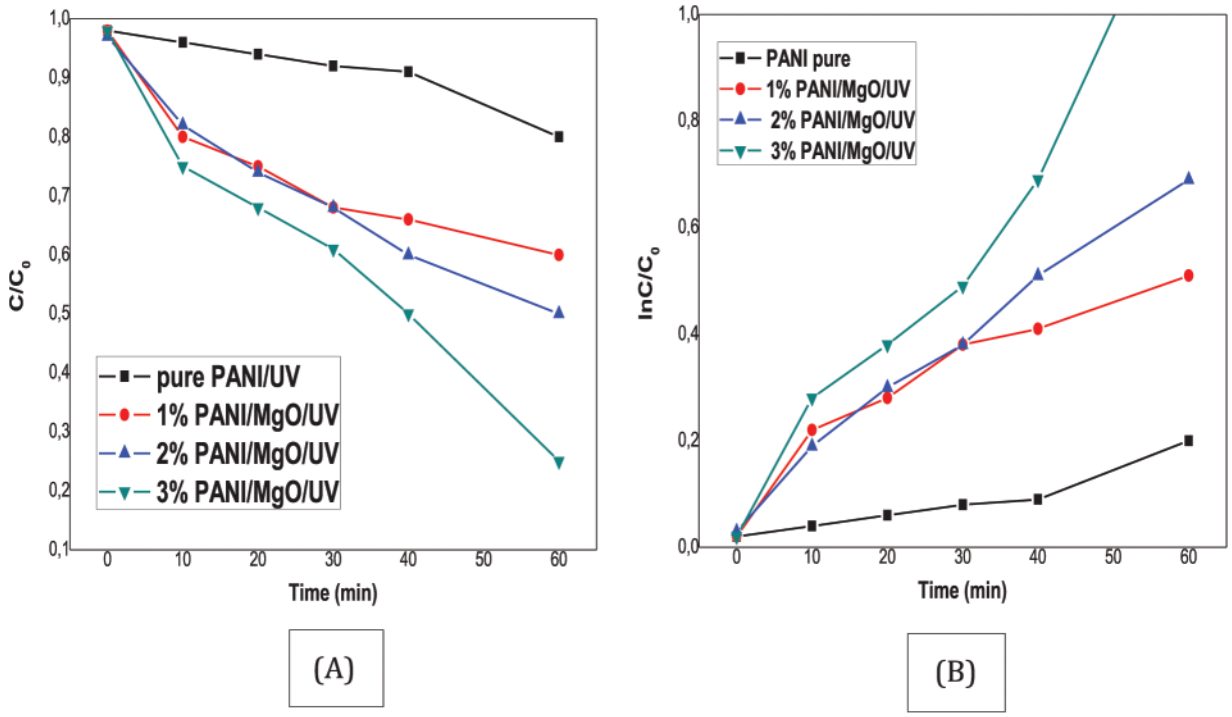

Figure 8: Decompositon of the dyes (MB) under UV light (A) C/C_0 (B) ln C/C_0 vs. time C% dye degration vs. time

3.5 Photodegradation Mechanism

When the PANI-MgO nanocomposite is exposed to visible light, the semi-conductive polyaniline efficiently absorbs photons, initiating a π-π^* transition state and subsequently generating electron-hole pairs.

Photogenerated are readily transferred to the conduction band of MgO due to the close energy alignment between the electrons and the conduction band of MgO [29,30]. The electrons in the conduction band (e^- CB) can be readily captured on the surface of the nanocomposites, Leading to the formation of. O^-_2 radicals or other reactive oxygen species.

Meanwhile, the holes remaining in the polyaniline (h^+ PANI) can react directly with H_2O or OH^- in the MB solution to produce HO radicals. Both O_2^- and HO radicals are highly reactive and effectively break down organic pollutants into less harmful substances, eventually converting them into H_2O and CO_2. Fig. 9 schematizes the mechanism of photodegradation.

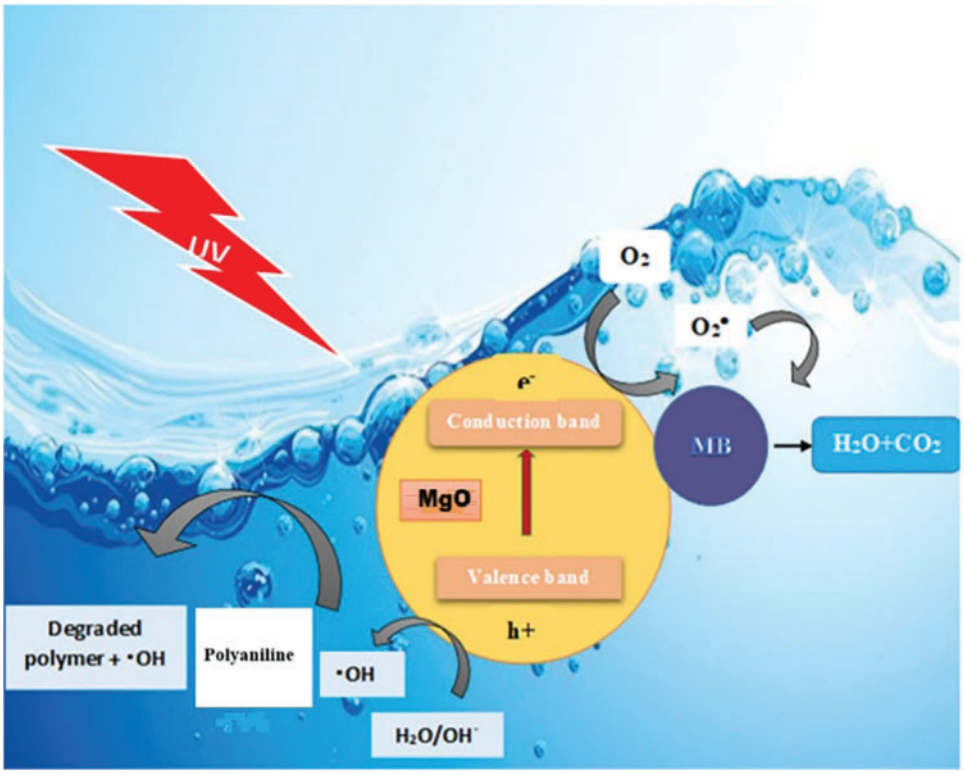

Figure 9: Schematic description of photocatalysis mechanism of PANI/MgO nanocomposites under visible light irradiation

As a result, the synthesized PANI-MgO nanocomposite exhibits superior photocatalytic activity under visible light compared to commercial MgO. The primary reactions are as follows:

$$PANI - MgO + hv \rightarrow *PANI - MgO \quad (R1)$$

$$* PANI - MgO \rightarrow PANI - MgO + e^-_{CB}/h^+_{CP} \quad (R2)$$

$$e^-_{CB} + O_2 \rightarrow \bullet O_2 \quad (R3)$$

$$H_2O + \bullet O_2^- \rightarrow \bullet OOH + OH^- \quad (R4)$$

$$2 \bullet OOH \rightarrow O_2 + H_2O_2 \quad (R5)$$

$$O_2 + 2H^+ + 2e^-_{CB} \rightarrow H_2O_2 \quad \text{(R6)}$$

$$H_2O_2 + \bullet O_2^- \rightarrow \bullet OH + OH^- + O_2 \quad \text{(R7)}$$

$$H_2O_2 + e^-_{CB} \rightarrow \bullet OH + OH^- \quad \text{(R8)}$$

Because polyaniline has C-C and C-H bonds, UV light is the sole source that may stimulate the photocatalytic degradation of PANI. It is suggested that the MB dye creates holes in the ground state on MgO nanostructures in PANI/MgO nanocomposites, which aids in PANI breakdown O_2H and OH. Attacking the polymeric chain, these oxygenated species are the first to cause PANI breakdown.

$$-(C_6H_5NH_2)-* + .OH \rightarrow (.C_6H_4NH)- + H_2O \quad \text{(R9)}$$

$$-(C_6H_5NH_2)-* + .O_2H \rightarrow (.C_6H_4NH)- + H_2O_2 \quad \text{(R10)}$$

Oxygen (O_2) molecules have an important central role in the degradation reactions of the PANI matrix. Once the become carbon-centered radicals embedded in the PANI polymer chain, their successive reactions lead to the chain splitting with the Incorporation of O_2 and the evolution of CO_2.

$$-(\cdot C_6H_4NH)- + O_2 \rightarrow -(C_6H_4(OO\cdot)\ NH)- \quad \text{(R11)}$$

$$-(C_6H_4(OO\cdot)\ NH)- + -(C_6H_5NH) \rightarrow -(C_6H_4(OOH)NH)- + -(\cdot C_6H_4NH)- \quad \text{(R12)}$$

$$-(C_6H_4(OOH)NH)- + hu \rightarrow (C_6H_4(O\cdot)\ NH)- + \cdot OH \quad \text{(R13)}$$

$$\cdot OH + \text{MB Dye} \rightarrow CO_2 + H_2O \quad \text{(R14)}$$

4 Conclusion

PANI/MgO NPs composite films were fabricated by the soft chemical process. The crystalline structure of PANI/MgO NPs composite films was confirmed using XRD, demonstrating the embedding of MgO NPs in the PANI matrix with a cubic phase. The AFM images revealed a significant change in the morphology of the PANI/MgO NPs composite films when the MgO concentration was increased. The optical transmittance shows that, for very low concentrations of MgO in PANI/MgO NPs composite films, there is a high transparency (close to 90%). This transmittance drops drastically when the concentration increases. This means that, for low concentration, PANI/MgO NPs can be used in optical devices. Finally, PANI/MgO NPs composite films were employed for the elimination of methylene blue dye from aqueous solutions. The results indicated an increase in dye elimination effectiveness with increasing concentrations of MgO nanoparticles in the composite films. The highest MB dye elimination reached 80% at 3%. The removal efficiency can be improved (i.e., approach 100%) if the concentration of MgO is further increased. Finally, the PANI/MgO NPs composite constitutes a good alternative material for photocatalysis.

Acknowledgement: None.

Funding Statement: The authors received no specific funding for this study.

Author Contributions: Malak Khannoucha: Investigation, MgO doped PANI composite fabrication, UV-visible measurement. Boubekeur Boudine: Investigation, Conceptualization, Methodology, Validation, Formal analysis, Writing—original draft, Writing—review & editing, Visualization. Imene Ameur: Investigation, MgO nanoparticles fabrication. Aouatef Dali: Investigation, Polyaniline fabrication. Ouahiba Halimi: Formal analysis. Miloud Sebais: Methodology, Formal analysis. Tahar Touam: AFM images measurement and analysis. All authors reviewed the results and approved the final version of the manuscript.

Availability of Data and Materials: The data shall be available from the first author on request.

Ethics Approval: Not applicable.

Conflicts of Interest: The authors declare no conflicts of interest to report regarding the present study.

References

1. Abbaci F, Nait-Merzoug A, Guellati O, Harat A, El Haskouri J, Delhalle J, et al. Bio/KOH ratio effect on activated biochar and their dye based wastewater depollution. J Anal Appl Pyrolysis. 2022;162:105452. doi:10.1016/j.jaap.2022.105452.
2. Nadeem MS, Munawar T, Mukhtar F, Rabbani AW, ur Rehman N, Mahmood K, et al. Facile synthesis of PANI and rGO supported Y/Pr Co-doped ZnO: boosted solar light-driven photocatalysis. Appl Phys A. 2023;129(6):450. doi:10.1007/s00339-023-06701-2.
3. Alasri TM, Ali SL, Salama RS, Alshorifi FT. Band-structure engineering of TiO_2 photocatalyst by AuSe quantum dots for efficient degradation of malachite green and phenol. J Inorg Organomet Polym Mater. 2023;33(6):1729–40. doi:10.1007/s10904-023-02604-0.
4. Fkiri A, Ali Saidani M, Chmangui A, Smiri LS. One-pot synthesis of copper-doped ZnO nanorods photocatalysts: degradation of diuron herbicide under simulated solar light. J Inorg Organomet Polym Mater. 2023;33(8):2523–30. doi:10.1007/s10904-023-02654-4.
5. Mary J, Vidya S. Photocatalysis and antibacterial activity studies of biopolymer incorporated green synthesized nano TiO2 without UV rays irradiation. J Inorg Organomet Polym Mater. 2023;33(3):707–30. doi:10.1007/s10904-023-02531-0.
6. Yakout SM, El-Zaidy ME. Blend nanoarchitectonics of nanocrystalline ZnO powder with Mn, Fe and co for superior visible light redox photocatalysis. J Inorg Organomet Polym Mater. 2023;33(9):2732–42. doi:10.1007/s10904-023-02692-y.
7. Guedri A, Zaabat M, Boudine B, Hafdallah A. Synthesis, characterization, structural, and optical properties of polyvinyl chloride/zinc oxide nanocomposite films for photocatalysis application. J Inorg Organomet Polym Mater. 2020;30(12):1–11.
8. Benhaoua A, Rahal A, Benhaoua B, Jlassi M. Effect of fluorine doping on the structural, optical and electrical properties of SnO_2 thin films prepared by spray ultrasonic. Superlattices Microstruct. 2014;70(207):61–9. doi:10.1016/j.spmi.2014.02.005.
9. Saravanan K, Ilayaraja M, Muthukrishnan P, Ananthakrishnan S, Ravichandiran P. As a highly magnetically recyclable Pd/Fe_3O_4 bifunctional catalyst on photocatalytic activity of nitrophenol degradation via the green route. J Inorg Organomet Polym Mater. 2024;34(2):584–92. doi:10.1007/s10904-023-02831-5.
10. Agha M, El-Kemary M, Oraby AH, Salim E. Efficient multilayers organic solar cells with hybrid interfacial layer-based P3HT and CuO nanoparticles. J Inorg Organomet Polym Mater. 2024;34(2):557–64. doi:10.1007/s10904-023-02829-z.
11. Rouabah N, Boudine B, Nazir R, Zaabat M, Sebais M, Halimi O, et al. Structural, optical and photocatalytic properties of PVC/CdS nanocomposites prepared by soft chemistry method. J Inorg Organomet Polym Mater. 2021;31(3):1102–10. doi:10.1007/s10904-020-01752-x.
12. Prasutiyo YJ, Manaf A, Hafizah ME. Synthesis of polyaniline by chemical oxidative polymerization and characteristic of conductivity and reflection for various strong acid dopants. J Phys: Conf Ser. 2020;1442(1):012003. doi:10.1088/1742-6596/1442/1/012003.
13. Saouti F, Belaaouad S, Cherqaoui A, Naimi Y. Polyaniline thin film prepared by electrochemical polymerization method. Biointerface Res Appl Chem. 2021;12(4):5523–33. doi:10.33263/BRIAC124.55235533.
14. Rajagopalachar S, Pattar J, Mulla S. Synthesis and characterization of plate like high surface area MgO nanoparticles for their antibacterial activity against *Bacillus cereus* (MTCC 430) and *Pseudomonas aeruginosa* (MTCC 424) bacterias. Inorg Chem Commun. 2022;144(17):109907. doi:10.1016/j.inoche.2022.109907.
15. Moritz K, Brachhold N, Küster F, Dudczig S, Schemmel T, Aneziris CG. Studies on the use of two different magnesia-carbon recyclates as secondary raw material for MgO-C refractories. Open Ceram. 2023;15:100426. doi:10.1016/j.oceram.2023.100426.

16. Yu S, Li Z, Han L, Zhao Y, Fu T. Biocompatible MgO film on titanium substrate prepared by sol-gel method. Rare Met Mater Eng. 2018;47(9):2663–7. doi:10.1016/S1875-5372(18)30206-6.
17. Mansoor S, Shahid S, Ashiq K, Alwadai N, Javed M, Iqbal S, et al. Controlled growth of nanocomposite thin layer based on Zn-doped MgO nanoparticles through sol-gel technique for biosensor applications. Inorg Chem Commun. 2022;142(1):109702. doi:10.1016/j.inoche.2022.109702.
18. Cui H, Wu X, Chen Y, Zhang J, Boughton RI. Influence of copper doping on chlorine adsorption and antibacterial behavior of mgo prepared by co-precipitation method. Mater Res Bull. 2015;61(11):511–18. doi:10.1016/j.materresbull.2014.10.067.
19. Zhang X, Wang X, He Y. Study on the crystal structure of magnesium ammonium carbonate tetrahydrate and its thermal decomposition to MgO. Inorg Chem Commun. 2023;148:110289. doi:10.1016/j.inoche.2022.110289.
20. Wang R, Zhou F, Wang J, Yang Y, Liu W. Enhanced secondary electron emission properties of Zn doped MgO thin films prepared by aerosol assisted chemical vapor deposition. Mater Sci Semicond Process. 2023;157:107323. doi:10.1016/j.mssp.2023.107323.
21. Lim HR, Jung SJ, Hwang TY, Lee J, Kim KH, Cho HB, et al. Electromagnetic wave absorption properties of Fe/MgO composites synthesized by a simple ultrasonic spray pyrolysis method. Appl Surf Sci. 2019;473:1009–13. doi:10.1016/j.apsusc.2018.12.222.
22. Luo J, Chen Y, Zhang X, Ma R, Huang H, Sun S, et al. Microwave-induced preparation of MgO-loaded N-rich porous biochar from marine biomass for efficient CO_2 capture and mechanism exploration via theoretical calculation. J Clean Prod. 2023;405:136915. doi:10.1016/j.jclepro.2023.136915.
23. Klubnuan S, Amornpitoksuk P, Suwanboon S. Structural, optical and photocatalytic properties of MgO/ZnO nanocomposites prepared by a hydrothermal method. Mater Sci Semicond Process. 2015;39:515–20. doi:10.1016/j.mssp.2015.05.049.
24. Dabhane H, Ghotekar S, Zate M, Kute S, Jadhav G, Medhane V. Green synthesis of MgO nanoparticles using aqueous leaf extract of Ajwain (*Trachyspermum ammi*) and evaluation of their catalytic and biological activities. Inorg Chem Commun. 2022;138(1):109270. doi:10.1016/j.inoche.2022.109270.
25. Devaraja PB, Avadhani DN, Nagabhushana H, Prashantha SC, Sharma SC, Nagabhushana BM, et al. Luminescence properties of MgO: Fe^{3+} nanopowders for WLEDs under NUV excitation prepared via propellant combustion route. J Radiat Res Appl Sci. 2015;8(3):362–73. doi:10.1016/j.jrras.2015.02.001.
26. Raj ILP, Revathy MS, Christy AJ, Chidhambaram N, Ganesh V, AlFaify S. Study on the synergistic effect of terbium-doped SnO_2 thin film photocatalysts for dye degradation. J Nanopart Res. 2020;22(12):359. doi:10.1007/s11051-020-05084-2.
27. Ameur I, Boudine B, Laidoudi M, Khennoucha M, Brien V, Horwat D, et al. Correction to: influence of magnesium doping on microstructure, optical and photocatalytic activity of zinc oxide thin films synthesis by sol-gel route. Appl Phys A. 2021;127(6):430. doi:10.1007/s00339-021-04523-8.
28. El-Hachemi B, Miloud S, Sabah M, Souad T, Zineddine O, Boubekeur B, et al. Structural, electrical and optical properties of PVC/ZnTe nanocomposite thin films. J Inorg Organomet Polym Mater. 2021;31(9):3637–48. doi:10.1007/s10904-021-01994-3.
29. Salzner U, Lagowski JB, Pickup PG, Poirier RA. Comparison of geometries and electronic structures of polyacetylene, polyborole, polycyclopentadiene, polypyrrole, polyfuran, polysilole, polyphosphole, polythiophene, polyselenophene and polytellurophene. Synth Met. 1998;96(3):177–89. doi:10.1016/S0379-6779(98)00084-8.
30. Snook JH, Samuelson LA, Kumar J, Kim YG, Whitten JE. Ultraviolet photoelectron spectroscopy of nanocrystalline TiO_2 films sensitized with (2,2'-bipyridyl) ruthenium (II) dyes for photovoltaic applications. Org Electron. 2005;6(2):55–64. doi:10.1016/j.orgel.2005.03.001.